Vol. **110** (2006) *ACTA PHYSICA POLONICA A* No. 2

Proceedings of the XXXV International School of Semiconducting Compounds, Jaszowiec 2006

Modeling of Semiconductor Nanostructures with next**nano**^{3}

S. Birner[a,*], S. Hackenbuchner[a], M. Sabathil[a], G. Zandler[a], J.A. Majewski[b], T. Andlauer[a], T. Zibold[a], R. Morschl[a], A. Trellakis[a] and P. Vogl[a]

[a]Walter Schottky Institute and Physics Depart., Technical University of Munich
Am Coulombwall 3, 85748 Garching, Germany
[b]Institute of Theoretical Physics, Warsaw University
Hoża 69, 00-681 Warszawa, Poland

next**nano**^{3} is a simulation tool that aims at providing global insight into the basic physical properties of realistic three-dimensional mesoscopic semiconductor structures. It focuses on quantum mechanical properties such as the global electronic structure, optical properties, and the effects of electric and magnetic fields for virtually any geometry and combination of semiconducting materials. For the calculation of the carrier dynamics a drift--diffusion model based on a quantum-mechanically calculated density is employed. In this paper we present an overview of the capabilities of next**nano**^{3} and discuss some of the main equations that are implemented into the code. As examples, we first discuss the strain tensor components and the piezoelectric effect associated with a compressively strained InAs layer for different growth directions, secondly, we calculate self-consistently the quantum mechanical electron density of a Double Gate MOSFET, then we compare the intersubband transitions in a multi-quantum well structure that have been obtained with a single-band effective mass approach and with an 8-band $\boldsymbol{k}\cdot\boldsymbol{p}$ model, and finally, we calculate the energy spectrum of a structure in a uniform magnetic field.

PACS numbers: 73.43.Cd, 73.21.Fg, 73.61.Ey, 77.65.Ly, 85.30.Tv, 73.40.Mr

1. Introduction

The quickly progressing technology of semiconductor quantum structures requires and depends on reliable predictive theoretical methods for systematically

*corresponding author; e-mail: stefan.birner@nextnano.de

improving, designing, and understanding the electronic and optical properties of such structures. Due to the increase in computing power and the simultaneous decrease of cost for fast processors and memory, computational physics is no longer a field of specialists (i.e. theorists) that have access to powerful supercomputers. Computer modeling nowadays has become a convenient tool for both, educational purposes as well as to support experimentalists while analyzing measured data or to design new experiments. The challenge is to make available to this audience a tool that covers the most important improvements that have been made over the past decades, i.e. to go beyond the simple "single-band effective-mass" model that is still widely used due to its simplicity [1]. More sophisticated models take into account the anisotropy and nonparabolicity of the electron and hole masses, usually employed within an 8-band $\boldsymbol{k} \cdot \boldsymbol{p}$ model. Strain is an important degree of freedom to optimize the electronic and optical properties of heterostructures. This involves a model to take into account deformation potentials as well as piezoelectric fields. Finally, the technologically important nitride materials crystallize in the wurtzite structure. This introduces more complexity into the equations in comparison to the simpler zinc blende materials. Additionally, pyroelectric fields have to be taken into account. Moreover, semiconductor layers can be grown not only on (001) oriented wafers but also along less symmetric crystallographic directions like [311]. These orientations not only require the rotation of the coordinate systems and the relevant equations, but make it also necessary to consider nonsymmetric displacement tensors as well as piezoelectric fields. Furthermore, during the past decade two-dimensional (2D) and three-dimensional (3D) quantum confinement has been studied intensively in quantum wires and quantum dots. Consequently, these heterostructures require 2D or 3D simulation environments [2] which go beyond simple self-written codes for 1D quantum wells. Finally, most of these structures require the application of a bias, and thus a model that calculates the current has to be implemented.

In this tutorial lecture the relevant physical models that are implemented in the software package next**nano**^{3} [3] will be described. next**nano**^{3} allows one to study the realistic electronic structure and optical properties of arbitrarily shaped 3D semiconductor nanostructures (diamond-type, zinc blende, and wurtzite materials and its alloys) and optoelectronic nanodevices under bias and its current density close to equilibrium. First, the strain is calculated within a continuum elasticity approach. Using band offsets and deformation potential theory, the new conduction and valence band edges are obtained. Then the multi-band Schrödinger, Poisson, and current equations have to be solved self-consistently, taking into account doping, piezo- and pyroelectric charges and excitonic effects. Finally, optical properties such as transition matrix elements can be calculated. Examples and applications such as multi-quantum wells, quantum wires, quantum dots, quantum-cascade lasers and type-II superlattices will be presented in this paper.

2. The next**nano**^{3} software

2.1. Program flow

The program flow of next**nano**^{3} can be summarized as follows. The user specifies the input using a text file that defines the geometry and the materials of the nanostructure, the contact bias, and all other information needed to describe the physical system under consideration. Then, in the initial phase, the program evaluates the bulk band structure of all constituent materials, performs a global strain calculation, and determines the new band edges and piezo- and pyroelectric charges. Subsequently, the Poisson equation, current equation, and multi-band Schrödinger equations are solved self-consistently. Finally, optical matrix elements can be computed. A database containing the material parameters for group IV and III–V materials in both, zinc blende and wurtzite crystal structures is provided. Template input files for various example structures are described online as tutorials [3] and are available on request. We note that a new version of the code (nextnano^{++}, written in the C^{++} programming language) is currently under development [4].

2.2. Strain and piezoelectricity

Heterostructures made of semiconductor materials with different lattice constants are subject to elastic deformations. Such deformations can be studied within a continuum mechanical model based on classical elasticity within the harmonic approximation, i.e. for small strains. As the lattice deformation changes drastically with the surface orientation (i.e. growth direction), an exact knowledge of the strain fields is of great importance for the interpretation of the experimental data and for the design and development of optoelectronic and electronic devices. Strain leads to piezoelectric effects, influences the conduction and valence band edges (including their degeneracies) and the $\boldsymbol{k \cdot p}$ Hamiltonian of Schrödinger equation. Therefore, strain is a very important "tool" for device engineers to alter the electronic and optical properties of semiconductor heterostructures. next**nano**^{3} calculates the strain prior to the Poisson, Schrödinger or current equations, i.e. strain is independent of all other equations and can thus be separated from the main part of the program.

The strain tensor $\varepsilon(\boldsymbol{x})$, i.e. the symmetrical part of the deformation tensor, is defined as

$$\varepsilon_{ij}(\boldsymbol{x}) = \frac{1}{2}\left(\frac{\mathrm{d}\boldsymbol{u}_i}{\mathrm{d}x_j} + \frac{\mathrm{d}\boldsymbol{u}_j}{\mathrm{d}x_i}\right) = \frac{1}{2}\left(\boldsymbol{u}_{ij} + \boldsymbol{u}_{ji}\right) = \varepsilon_{ji}, \tag{1}$$

where $i, j = \{1, 2, 3\}$ and $\boldsymbol{u(x)}$ describes the displacement due to lattice deformations. The strain tensor ε is symmetric whereas the distortion tensor $\boldsymbol{u}$ is in general not symmetric (see Fig. 1). The diagonal elements of the strain tensor measure the extensions per unit length along the coordinate axes (positive values mean tensile strain, negative values — compressive strain), i.e. the lengths of the considered volume element change while the angles remain constant. In contrast,

the off-diagonal elements measure the shear deformations where the angles change and the volume remains constant. As the (3×3) matrix ε is real and symmetric, it can always be diagonalized by an appropriate orthogonal transformation. The resulting diagonal matrix must not necessarily coincide with the crystal or simulation coordinate system. The trace of the strain tensor $\mathrm{Tr}(\varepsilon)$ is equal to the hydrostatic strain, i.e. the change in volume. The strain tensor components are obtained by minimizing the elastic energy

$$E = \frac{1}{2} \int_V C_{ijkl} \varepsilon_{ij} \varepsilon_{kl} \mathrm{d}V, \tag{2}$$

where C_{ijkl} is the forth-ranked elastic stiffness tensor.

The piezoelectric polarization is a consequence of strain. In zinc blende materials, this polarization with respect to the *crystal coordinate system* is given by

$$\boldsymbol{P}^{\mathrm{pz}}(\boldsymbol{x}) = e_{14} \begin{pmatrix} 2\varepsilon_{yz} \\ 2\varepsilon_{xz} \\ 2\varepsilon_{xy} \end{pmatrix}, \tag{3}$$

where e_{14} is the piezoelectric constant. The spatial variation of $\boldsymbol{P}^{\mathrm{pz}}$ leads to piezoelectric charges and the resulting piezoelectric field is obtained by solving the Poisson equation (9). Figure 1 shows the strain tensor components with respect to the crystal coordinate system for a compressively strained InAs layer grown pseudomorphically on InP for different growth directions. The maximum value for the volume deformation (i.e. extremal value of the hydrostatic strain) is obtained for the [111] growth direction. In zinc blende heterostructures grown along the [100] direction only diagonal strain components occur but any other growth direction ex-

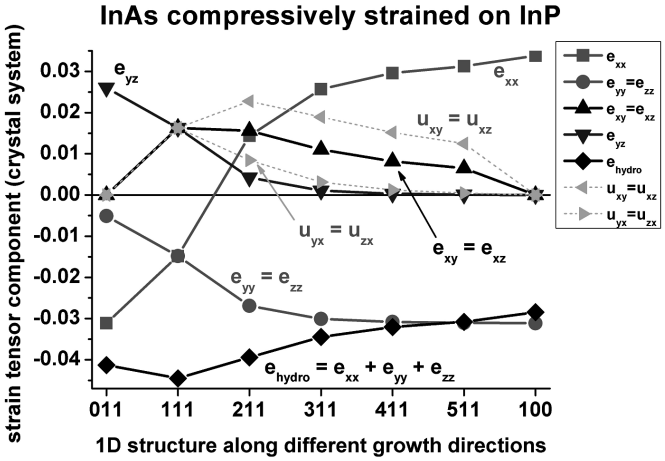

Fig. 1. Strain tensor components for a compressively strained InAs layer grown pseudomorphically on InP for different growth directions. Note that [100] growth direction corresponds to $[\infty 11]$ and only for this growth direction all off-diagonal strain tensor components are zero. The maximum value for the volume deformation (hydrostatic strain) is obtained for [111] (the lines are a guide to the eye).

hibits off-diagonal strain components. For heterostructures grown along the [011] direction, where ε_{yz} is nonzero, the piezoelectric polarization is oriented in the plane perpendicular to the growth direction, thus no piezoelectric field is obtained along the growth direction. For all other growth directions, a piezoelectric field along the growth direction is obtained because for a general growth direction $\boldsymbol{P}^{\mathrm{pz}}$ has components both parallel and perpendicular to the growth axis. Thus, strain and piezoelectricity can be used to alter and optimize the electronic and optical properties of quantum wells, wires, and dots by varying both the energy levels and the spatial extensions of the wave functions. We note that care should be taken on the definition of the piezoelectric sign. For heterostructures, the sign convention of the IEEE standard [5] — e_{14} is always positive — is not strictly applicable, thus a slight modification is needed: The sign of the piezoelectric constant is taken as positive if a positive charge is induced in the positive direction of the axis under a positive (tensile) stress. In next**nano**^{3} we define as the positive [111] direction the one from cation to anion. In this case the piezoelectric constant can be both positive (AlP, InP) and negative (AlAs, InAs).

2.3. Schrödinger equation

The so-called envelope function approximation (EFA) based on the $\boldsymbol{k}\cdot\boldsymbol{p}$ method is used to calculate the energy levels and wave functions of electrons and holes. In the single-band approximation the Hamiltonian for the electrons reads

$$-\frac{\hbar^2}{2}\left[\nabla_i\cdot\left(\frac{1}{m_{\mathrm{e}}(\boldsymbol{x})}\right)_{ij}\nabla_j + E_{\mathrm{c}}(\boldsymbol{x})\right]\psi_n^{\mathrm{c}}(\boldsymbol{x}) = E_n^{\mathrm{e}}\psi_n^{\mathrm{e}}(\boldsymbol{x}), \tag{4}$$

where the spatially varying effective mass tensor $(1/m)_{ij}$ can be calculated taking into account modifications of the masses due to the local strain field. E_{c} is the conduction band edge that is obtained by diagonalizing the 8-band $\boldsymbol{k}\cdot\boldsymbol{p}$ Hamiltonian and thus includes the shifts and splittings due to strain and deformation potentials, as well as the electrostatic potential that is obtained from the Poisson equation. The three single-band Schrödinger equations for the heavy, light, and split-off holes are similar. The description of the 8-band $\boldsymbol{k}\cdot\boldsymbol{p}$ model that is implemented into next**nano**^{3} is beyond the scope of this article. It is described in Ref. [6] for strained zinc blende and in Ref. [7] for strained wurtzite materials.

2.4. Carrier transport

To study the electronic structure and carrier transport under an applied bias a quantum-drift-diffusion method is used [8] which uses the first moment of the Boltzmann equation to determine the current and quantum mechanics to calculate the carrier density. In many nanostructures, the current $\boldsymbol{j}(\boldsymbol{x})$ is limited by several heterobarriers and therefore very small. In such a situation, it is reasonable to assume that the carriers are close to thermodynamic equilibrium. For a unipolar device and in the absence of recombination or generation, the basic equations then read

$$\boldsymbol{j}(\boldsymbol{x}) = \mu(\boldsymbol{x}) n(\boldsymbol{x}) \nabla E_{\mathrm{F},n}, \tag{5}$$

$$\nabla \cdot \boldsymbol{j}(\boldsymbol{x}) = 0, \tag{6}$$

$$n(\boldsymbol{x}) = \sum_i |\psi_i(\boldsymbol{x})|^2 f\left(\frac{E_i - E_{\mathrm{F},n}}{k_{\mathrm{B}}T}\right), \tag{7}$$

where $n(\boldsymbol{x})$ is the carrier density (that has to take into account the spin and valley degeneracies), ψ_i — the wave function and E_i — the energy of eigenstate i that have been obtained from solving the Schrödinger equation, $E_{\mathrm{F},n}$ is the quasi-Fermi level of the charge carrier type, and μ — the mobility. Let us note that the quantum states E_i get occupied nonuniformly in this model which is only meaningful if the potential varies slowly and the total current through the device is small. Recently, a detailed assessment of this model has been performed by comparing it with fully self-consistent nonequilibrium Green function (NEGF) calculations [9]. As an example, we present in Fig. 2 the results of a Double Gate (DG) MOSFET with an undoped Si channel having the length of 25 nm and the width of 5 nm that is embedded between two heavily n-doped Si regions of length 10 nm (doping concentration 1×10^{20} cm^{-3}) that are connected to source and drain

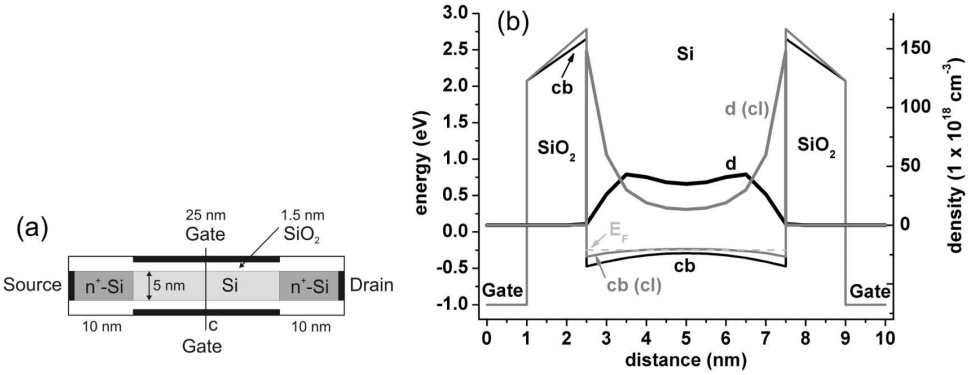

Fig. 2. (a) Schematic of a Double Gate MOSFET with an undoped Si channel having the length 25 nm and the width 5 nm that is embedded between two heavily n-doped Si regions of length 10 nm that are connected to source and drain contacts. The oxide thickness is 1.5 nm and the gate length is 25 nm. The vertical line labeled "c" is a cut through the middle of the device. (b) The figure shows a cut through the Double Gate MOSFET at the vertical line "c" of Fig. 2a. The conduction band edge ("cb"), the Fermi level (E_{F}) and the quantum mechanically calculated electron density ("d") at an applied source drain voltage $V_{\mathrm{SD}} = 0.5$ V and a gate voltage of $V_{\mathrm{SG}} = 1.0$ V (open channel). For comparison, the classical results are also plotted where the Fermi level is practically identical to the quantum mechanical case, the classical conduction band edge is labeled with "cb (cl)" and the classical electron density with "d (cl)". The densities "d" and "d (cl)" refer to the density axis on the right whereas all other lines refer to the left axis.

contacts. The oxide thickness is 1.5 nm and the gate length is 25 nm. Figure 2b shows a cut through the DG MOSFET at the vertical line "c" of Fig. 2a, where the conduction band edge, the Fermi level, and the quantum mechanically calculated electron density for the self-consistent solution of the 2D Schrödinger, Poisson, and current equations at an applied source drain voltage $V_{\mathrm{SD}} = 0.5$ V and a gate voltage of $V_{\mathrm{SG}} = 1.0$ V (open channel) are plotted. For comparison, the classical results are also shown (self-consistent solution of the 2D Poisson and current equations). The Fermi level is practically identical to the quantum mechanical case whereas the conduction band edges differ slightly. The most significant difference, however, is attributed to the electron densities. Due to the large oxide barrier, the wave functions of the electrons tend to zero at the oxide/silicon interface, and thus the quantum mechanically calculated electron density is almost zero at this interface. In contrast, in the classical calculation the maximum of the electron density occurs at the oxide/silicon interface which clearly does not correspond to the physical reality. Furthermore, depending on the width of the Si channel, the quantum mechanical density can have different shapes because the larger the Si width, the more eigenfunctions can be occupied. A comparison of the quantum mechanical and classical densities as a function of Si channel width can be found in Ref. [10]. The mobility in this MOSFET has been calculated by a simple standard model that takes into account the scattering of the carriers by charged impurity ions (ionized impurity scattering). Due to the strong quantum mechanical confinement in Nano-MOSFETs, usually quantum correction models are applied to avoid the unphysical high densities at SiO_2/Si interfaces. However, although these models can reproduce the drive current reduction, the carrier density shows only poor agreement with rigorous quantum mechanical calculations [10] because the shape of the quantum density depends critically on the applied gate voltage. Our approach takes into account the individual wave functions and is thus suited also for very general devices having more complicated geometries that are far beyond a quantum correction model. To understand, how the shape of the quantum mechanical density of Fig. 2b is obtained, one can analyze the square of the wave functions in Fig. 3 that contribute to the density in the middle of the device. All other wave functions, especially the ones in the doped regions are not shown. Because of the different orientations of the ellipsoidal effective mass tensors, there are three Schrödinger equations that have to be solved each time for the electrons, where the following effective mass tensor components m_{xx}, m_{yy} enter into the Hamiltonian $\hat{H}(x, y)$:

A) transversal mass oriented along x, longitudinal mass oriented along y direction,

B) transversal masses oriented along x and y directions,

C) longitudinal mass oriented along x, transversal mass oriented along y direction.

The longitudinal mass tensor component $m_{\mathrm{l}} = 0.916 m_0$ is larger than the transver-

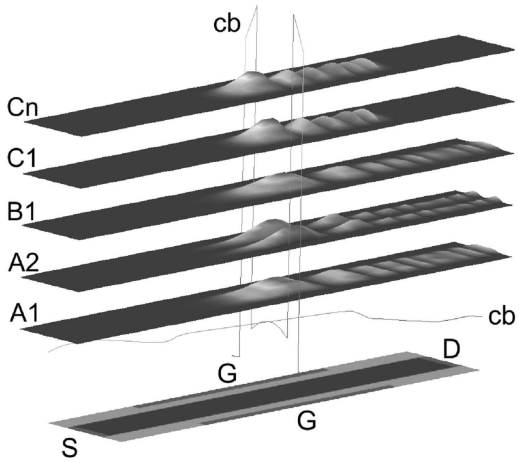

Fig. 3. At the bottom, a schematic of the MOSFET is shown (S = source, D = drain, G = gate). The conduction band edges (labeled "cb") of one vertical and one horizontal cut through the middle of the device of Fig. 2a are shown. The probability amplitudes of the eigenstates ("A1", "A2", "B1", "C1", "Cn") are discussed inside the text. The source drain voltage is $V_{\mathrm{SD}} = 0.5$ V and the gate voltage is $V_{\mathrm{SG}} = 0.7$ V (open channel).

sal mass tensor component $m_{\mathrm{t}} = 0.190 m_0$. As in the case of a standard MOSFET, where the electron ground state is the one with the longitudinal mass oriented perpendicular to the Si/SiO_2 interface, the same applies to a DG MOSFET, i.e. the first subband is the one where the longitudinal mass is oriented perpendicular to the Si/SiO_2 interface (labeled "A1") in Fig. 3. "A2" is the second subband. These two states are below the Fermi level and thus dominate the quantum mechanical density. Combining the shape of the probability amplitudes of "A1" and "A2", one can understand the shape of the quantum mechanical density shown in Fig. 2b. If only "A1" is occupied, the quantum mechanical density would have only one maximum in the center (not shown) instead of two maxima off-the-center as in Fig. 2b. The state "B1", whose energy is above the Fermi level, corresponds to the first subband of the Schrödinger equation, where both of the transversal masses are oriented in the plane of the DG MOSFET. Finally, the states "C1" and "Cn" correspond to subbands, where the longitudinal mass is oriented parallel to the Si channel. They also lie above the Fermi level. "B1" and "C1" have nearly identical energies. The square of the wave function "Cn" is zero in the middle of the device, i.e. it does not contribute to the density in the middle of the device, but it contributes to the density in close vicinity to the middle of the device. The mass tensor component $m_{zz}(x, y)$ does not enter the Hamiltonian $H(x, y)$ but it is used to calculate the quantum mechanical density which is proportional to $\sqrt{m_{zz}(x, y)}$ for such a 2D geometry. To conclude, the calculated quantum mechanical density depends in a very complicated way on the device geometry, the strength of the quantum confinement, the orientation of the mass tensor components, and the

spatially varying Fermi levels. Applying a gate voltage can alter the shape of the quantum density significantly because different shapes of probability amplitudes get occupied.

2.5. Semiconductor/electrolyte systems

The methodology of next**nano**^{3} can be straightforwardly extended to include electrolytes and the effects at semiconductor/electrolyte and oxide/electrolyte interfaces. Such nanostructures are gaining importance due to their large potential in commercial applications, like protein or *p*H sensors (bio-chips). An electrolyte is an aqueous solution containing dissolved ions that result from the dissociation of salts, e.g. NaCl (Na^+ Cl^-), $CaCl_2$ (Ca^{2+} Cl^- Cl^-). The *p*H value of this solution is related to concentration of H_3O^+ and OH^- ions. Such sensor systems (ion-selective field effect transistors, ISFETs) usually consist of a 2D electron (or hole) gas (2DEG, 2DHG) in the semiconductor region, where a source-drain voltage is applied in the 2DEG plane. The measured source-drain current obviously depends on the electron density in the 2DEG. The goal is to influence the electron density in the 2DEG through a change in the electrostatic potential by the charge distribution inside the electrolyte and at the oxide/electrolyte interface in a reproducible manner, i.e. the electrolyte acts as a gate. The charge density inside the electrolyte at the position $\boldsymbol{x}$ is given by

$$\rho(\boldsymbol{x}) = \sum\nolimits_{i=l}^{n} z_i e c_{i,0} \exp\left(-\frac{z_i e(\phi(\boldsymbol{x}) - U_\mathrm{G})}{k_\mathrm{B}T}\right), \tag{8}$$

where z_i is the ion valency, e is the positive elementary charge, $c_{i,0}$ is the bulk concentration of the ion species i, $k_\mathrm{B}T$ is the thermal energy at temperature T and U_G is the bulk electrolyte potential (which can be varied by a gate electrode). $\phi(\boldsymbol{x})$ is the electrostatic potential that is obtained by solving self-consistently the nonlinear Poisson–Boltzmann equation in the overall device, i.e. in both the electrolyte as well as in the semiconductor region

$$\nabla \cdot [\varepsilon_0 \varepsilon(\boldsymbol{x}) \nabla \phi(\boldsymbol{x})] = -\rho(\boldsymbol{x}, \phi), \tag{9}$$

where $\varepsilon_0\varepsilon$ is the dielectric constant at position $\boldsymbol{x}$, ε_0 is the permittivity of vacuum and ε is the relative permittivity of either the electrolyte or any of the semiconductor materials. Interface reactions can be taken into account by the so-called *site-binding model* for amphoteric oxide surfaces [11, 12], where the adsorption or dissociation of H^+ and OH^- ions at oxide/electrolyte interfaces lead to interface charge densities which depend on both, the electrostatic potential at the interface and the *p*H value of the electrolyte. These interface densities simply have to be included to the charge density ρ in Eq. (9). A more detailed description of the site-binding model can be found in Ref. [13] and references therein. An example of such a device could be a silicon nanowire that is surrounded by an electrolyte and the specific charge distribution in the electrolyte may arise from protein binding to the semiconductor surface, where the surface is functionalized with a lipid layer so that proteins can specifically bind to the headgroups of the lipids on the surface.

The self-consistent calculation of the spatial charge and potential distribution for different ion concentrations in the electrolyte can be used to interpret experimental data and to optimize the sensitivity of these devices. A highly promising material system for such kind of devices are nitride-based ion sensors like AlGaN/GaN because they are not toxic (in comparison to GaAs-based ion sensors), possess a chemically inert oxide surface and they are extremely sensitive to changes of the surface charge or surface potential due to their large built-in piezo- and pyroelectric fields.

2.6. Energy levels in unipolar devices based on intersubband transitions

Figure 4 shows a comparison between the widely used single-band effective--mass model and the more sophisticated 8-band $\boldsymbol{k} \cdot \boldsymbol{p}$ model for the electron eigen-

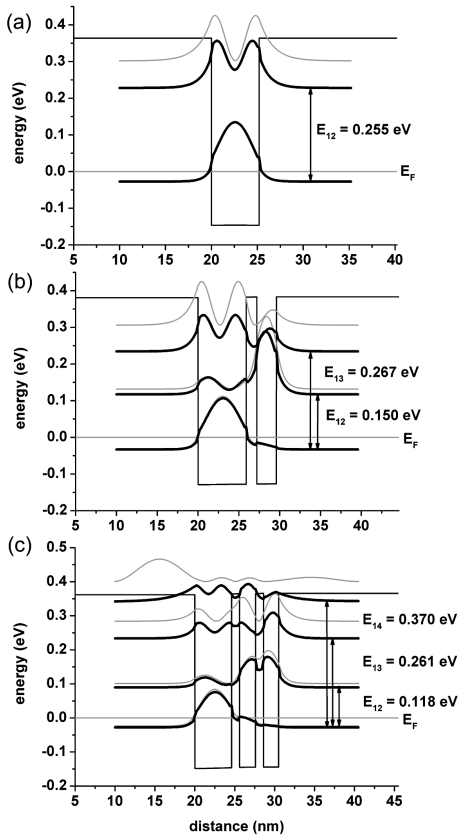

Fig. 4. Lowest electron eigenstates of a single (a), double (b), and triple quantum well (c) calculated with an 8-band $\boldsymbol{k} \cdot \boldsymbol{p}$ model (thick, black lines). The thin, grey lines show the eigenstates obtained with a single-band effective-mass model. Only for the ground state, these two models are in good agreement but differ significantly for the higher-lying states. In all three cases, the ground state is lying below the Fermi level $E_{\mathrm{F}} = 0$ eV and thus dominates the charge density.

states of a single (a), double (b) and triple quantum well (c). The geometry, material parameters, and doping profiles of these structures are based on Ref. [14] with the exception of the $\boldsymbol{k}\cdot\boldsymbol{p}$ parameters which are taken from Ref. [15]. The QW material consists of $In_{0.53}Ga_{0.47}As$ and the barrier material of $Al_{0.48}In_{0.52}As$. Both materials are assumed to be unstrained with respect to the InP substrate. One can clearly see that for the ground state, the single-band approximation is acceptable. However, the single-band model overestimates intersubband transition energies. Consequently, for unipolar devices that are based on intersubband transitions like quantum cascade lasers (QCL) or quantum well infrared photodetectors (QWIP), a model that takes into account the nonparabolicity of the effective mass is mandatory to get correct energies for the higher-lying states. Our calculated energies for intersubband transitions are in good agreement with the experimental measurements and theoretical calculations of Ref. [14]. We note that for strained structures where the nonparabolicity and anisotropy of the effective masses can change dramatically, the deviations between the single-band and the $\boldsymbol{k}\cdot\boldsymbol{p}$ model are even more pronounced. An estimate for the probability of intersubband transitions in QCLs or QWIPs between initial state i and final state f can be obtained by evaluating the intersubband dipole moments M_{fi}

$$|M_{fi}| = \left| \int \psi_f^*(z) p_z \psi_i(z) \mathrm{d}z \right| = \left| -\mathrm{i}\hbar \int \psi_f^*(z) \frac{\mathrm{d}}{\mathrm{d}z} \psi_i(z) \mathrm{d}z \right| . \tag{10}$$

2.7. Energy spectrum of heterostructures in a magnetic field

Quantum dots that are subject to a magnetic field are an interesting research subject since many years. A popular approach to study the energy spectrum of such systems theoretically is the assumption of a 2D parabolic confinement potential that is subject to a perpendicularly oriented magnetic field which introduces a further parabolic confinement, thus making it possible to solve this equation analytically [16]. Obviously, such an approach only makes sense for circularly shaped quantum dots. However, due to piezoelectric fields that arise because of strain fields in realistic self-assembled quantum dots, this circular symmetry is definitely not present in real systems. Furthermore, the above-mentioned 2D model neglects completely the quantum confinement along the growth direction. Consequently, it would be desirable to have a more predictive model that takes into account the realistic electronic structure of quantum dots of arbitrary shape, including strain, deformation potentials and piezoelectric effects, and then apply the magnetic field and calculate the energy levels. Governale et al. [17] showed how to discretize the single-particle Schrödinger equation on a 2D homogeneous grid in a gauge-invariant way assuming a constant effective mass tensor. We extended their method to spatially varying effective masses and to an inhomogeneous grid [18] and are now able so solve the Schrödinger equation in three dimensions including a uniform magnetic field. The Hamilton operator of Eq. (4) has to be modified to include the magnetic field and is now given by

$$\hat{H} = -\frac{\hbar^2}{2}\left[(\nabla_i + \mathrm{i}gA_i)\cdot\left(\frac{1}{m_\mathrm{e}(x)}\right)_{ij}(\nabla_j + \mathrm{i}gA_j)\right], \tag{11}$$

where $g = e/\hbar$ and $\boldsymbol{A}(\boldsymbol{x})$ is the vector potential which is discretized in the symmetric gauge

$$\boldsymbol{A}(\boldsymbol{x}) = -\frac{1}{2}\boldsymbol{x}\times\boldsymbol{B}. \tag{12}$$

As a benchmark for our method, we chose to recalculate the well-known Fock–Darwin spectrum [16] which is an analytical result. We note that our result is completely numerical, i.e. we solve the single-particle 2D Schrödinger equation in the (x, y) plane for a 2D parabolic confinement potential, where the uniform magnetic field is applied along the z direction. The parabolic confinement had been chosen so that the energy separation between the states is $\hbar\omega_0 = 3$ meV (without magnetic field), where ω_0 is the oscillator frequency of the parabolic confinement. The effective mass had been assumed to be constant ($m_\mathrm{e} = 0.067m_0$, electron effective mass of GaAs). Without magnetic field, and neglecting the two-fold spin degeneracy, the ground state is not degenerate, the second level is two-fold degenerate, the third level three-fold, and so on, as can be seen from the analytical result of the energy spectrum

$$E_{n,l} = (2n + |l| - 1)\hbar\omega_0, \tag{13}$$

where $n = 1, 2, 3, \ldots$ is the radial quantum number and $l = 0, \pm1, \pm2, \ldots$ the angular momentum quantum number. If the magnetic field is present, the eigenstates look as follows

$$E_{n,l} = (2n + |l| - 1)\hbar\left(\omega_0^2 + \frac{1}{4}\omega_\mathrm{c}^2\right)^{1/2} - \frac{1}{2}l\hbar\omega_\mathrm{c}, \tag{14}$$

where $\omega_\mathrm{c} = eB/m_\mathrm{e}$ is the cyclotron frequency, and thus the degeneracy of the 2D harmonic oscillator is lifted as can be seen in the calculated energy spectrum (Fig. 5), where the energy levels are plotted as a function of the magnetic field magnitude. A more detailed discussion of this energy spectrum can be found in [16]. We conclude that our numerical calculations are in perfect agreement to the analytical results, and therefore, our method can be straightforwardly applied to realistic, 3D confinement potentials to obtain the energy spectrum of the transitions of quantum dots subject to a magnetic field.

3. Conclusions

We briefly mentioned some of the main equations that are implemented into the next**nano**^{3} software which is an extremely useful tool to study the electronic and optical properties of one-, two- and three-dimensional semiconductor nanostructures. We have shown how any software of this kind can easily be extended to describe semiconductor/electrolyte systems. Finally, we presented four simulation examples. In the first example we calculated the strain tensor components of a compressively strained InAs layer for different growth directions and discussed the

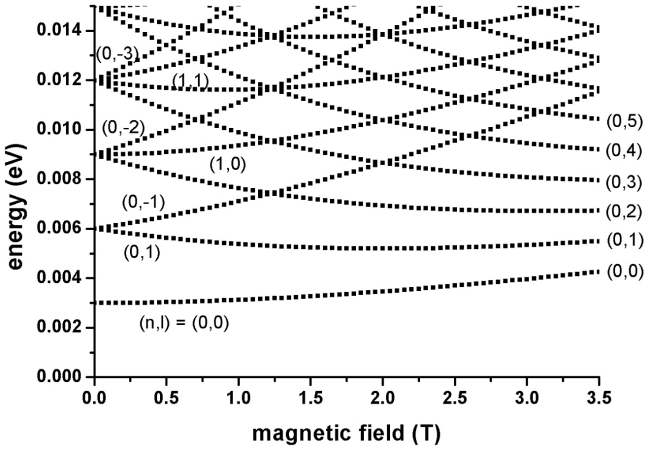

Fig. 5. Calculated single-particle energy levels of a two-dimensional parabolic confinement potential ($\hbar\omega_0 = 3$ meV) as a function of magnetic field magnitude (Fock–Darwin spectrum). The states can be labeled by (n, l), which refers to the radial quantum number (n) and the angular momentum quantum number (l).

associated piezoelectric effects. In the second example we demonstrated that for Nano-MOSFETs the quantum mechanical density significantly differs from the classical density. Then we showed that for the accurate modeling of unipolar devices based on intersubband transitions, a model that goes beyond the single--band approximation — like the multi-band $\boldsymbol{k} \cdot \boldsymbol{p}$ model — is mandatory. Finally, we demonstrated how to calculate the Fock–Darwin energy spectrum of a 2D parabolic confinement potential in a magnetic field.

Acknowledgment

S.B. acknowledges useful discussions with M. Povolotskyi and financial support by the EXIST-SEED program "University-based start-ups" of the German Federal Ministry of Education and Research.

References

[1] e.g. G. Snider's "1D Poisson" program available at http://www.nd.edu/ gsnider/.

[2] e.g. O. Stier, M. Grundmann, D. Bimberg, *Phys. Rev. B* **59**, 5688 (1999).

[3] The next**nano**^{3} software can be obtained from http://www.wsi.tum.de/nextnano3 and http://www.nextnano.de.

[4] A. Trellakis, T. Zibold, T. Andlauer, S. Birner, R.K. Smith, R. Morschl, P. Vogl, *J. Comp. Elec.*, in print.

[5] *IEEE Standard on Piezoelectricity*, ANSI/IEEE Std **176-1987**, 227 (1987).

[6] T.B. Bahder, *Phys. Rev. B* **41**, 11992 (1990).

[7] S.L. Chuang, C.S. Chang, *Phys. Rev. B* **54**, 2491 (1996).

[8] M. Sabathil, S. Hackenbuchner, J.A. Majewski, G. Zandler, P. Vogl, *J. Comp. Elec.* **1**, 81 (2002).

[9] T. Kubis, P. Vogl, *J. Comp. Elec.*, in print.

[10] R. Entner, A. Gehring, T. Grasser, S. Selberherr, in: *Proc. IEEE 27th Intern. Spring Seminar on Electronics Technology*, Vol. 1, Ed. P. Philippov, Sofia 2004, p. 114.

[11] P. Bergveld, *IEEE Trans. Biomed. Eng.* **17**, 70 (1970).

[12] T.W. Healy, L.R. White, *Adv. Colloid Interface Sci.* **9**, 303 (1978).

[13] M. Bayer, C. Uhl, P. Vogl, *J. Appl. Phys.* **97**, 033703 (2005).

[14] C. Sirtori, F. Capasso, J. Faist, S. Scandolo, *Phys. Rev. B* **50**, 8663 (1994).

[15] I. Vurgaftman, J.R. Meyer, L.R. Ram-Mohan, *J. Appl. Phys.* **89**, 5815 (2001).

[16] L.P. Kouwenhoven, D.G. Austing, S. Tarucha, *Rep. Prog. Phys.* **64**, 701 (2001).

[17] M. Governale, C. Ungarelli, *Phys. Rev. B* **58**, 7816 (1998).

[18] S. Hackenbuchner, in: *Selected Topics of Semiconductor Physics and Technology*, Eds. G. Abstreiter, M.-C. Amann, M. Stutzmann, P. Vogl, Vol. 48, Walter Schottky Institute, TU Munich, Munich 2002, p. 132.